

## Rapid inversion of 2-D geoelectrical data by multichannel deconvolution

Ingelise Møller\*, Bo H. Jacobsen<sup>‡</sup>, and Niels B. Christensen<sup>‡</sup>

### ABSTRACT

Modern geoelectrical data acquisition systems can record more than 100 000 data values per field day. Despite the growth in computer power and the development of more efficient numerical algorithms, interpreting such data volumes remains a nontrivial computational task. We present a 2-D one-pass inversion procedure formulated as a multichannel deconvolution. It is based on the equation for the electrical potential linearized under the Born approximation, and it makes use of the 2-D form of the Fréchet derivatives evaluated for the homogeneous half-space. The inversion is formulated in the wavenumber domain so that the 2-D spatial problem decouples into many small 1-D problems. The resulting multichannel deconvolution algorithm is very fast and memory efficient. The inversion scheme is stabilized through covariance matrices representing

the stochastic properties of the earth resistivity and data errors.

The earth resistivity distribution is assumed to have the statistical characteristics of a two-parameter, self-affine fractal. The local apparent amplitude and fractal dimension of the earth resistivity are estimated directly from geoelectrical observations. A nonlinearity error covariance matrix is added to the conventional measurement error covariance matrix. The stochastic model for the dependence of nonlinearity error on electrode configuration as well as resistivity amplitude and fractal dimension is determined pragmatically through nonlinear simulation experiments. Tests on synthetic examples and field cases including well control support the conclusion that for long data profiles this method automatically produces linearized resistivity estimates which faithfully resolve the main model features.

### INTRODUCTION

Over the past decade 2-D geoelectrical data for combined sounding and profiling have seen extended use. The data volume collected per field day has increased with the advent of computerized data acquisition systems (e.g., Griffiths and Turnbull, 1985; Dahlin, 1996), several of which are commercially available. Data volumes are also increased by data acquisition techniques using moving electrodes (Sørensen, 1996; Panissod et al., 1998), which can produce more than 10 line kilometers of densely sampled, multiconfiguration data per day. With these developments, the geoelectrical method is now well suited to large-scale mapping of groundwater (Christensen and Sørensen, 1998; Møller and Sørensen, 1998) as well as archeological/geotechnical applications (Panissod et al., 1998).

However, interpretation of large amounts of profile data demands efficient 2-D inversion procedures. Over the years, a variety of 2-D geoelectrical inversion procedures have been proposed, most of them based on iterative linearized inversion (e.g., Sasaki, 1989; LaBrecque et al., 1996).

Two-dimensional inversion of large data sets using iterative inversion is computationally expensive because partial derivatives must be calculated and because large linear systems of equations must be solved.

We present an approximate one-pass 2-D inversion procedure which speeds up the inversion by orders of magnitude relative to iterative linearized procedures. The method is formulated as a multichannel deconvolution and is developed from the approach presented by Li and Oldenburg (1992) for 3-D data. The 2-D problem is solved in the wavenumber domain. Regularization is controlled through pragmatically determined covariance matrices describing the correlated covariance properties of the earth resistivity as well as data errors. The spatial variability of the earth resistivity distribution is represented by a two-parameter, self-affine fractal. Empirical relations for estimating amplitude and fractal dimension directly from data are found through simulation experiments.

The nonlinear forward problem and the linear inversion computation present a problem for all one-pass algorithms

Manuscript received by the Editor April 21, 1999; revised manuscript received September 27, 2000.

\*Formerly University of Aarhus, Department of Earth Sciences, Geophysical Laboratory, Aarhus, Denmark, presently Geological Survey of Denmark and Greenland, Thoravej 8, DK-2400 Copenhagen, Denmark. E-mail: ilm@geus.dk.

‡University of Aarhus, Department of Earth Sciences, Geophysical Laboratory, Finlandsgade 8, 8200 Aarhus N, Denmark. E-mail: bo@geo.aau.dk; geofnbc@geo.aau.dk.

© 2001 Society of Exploration Geophysicists. All rights reserved.

(e.g., Li and Oldenburg, 1992; Loke and Barker, 1995). We quantify this problem in terms of the nonlinearity error, defined as the difference between the actual nonlinear response and the linearized response. With increasing subsurface resistivity contrast, this extra error term becomes important relative to the measurement noise and also relative to the total response. Disregarding this nonlinearity error in one-pass stochastic inversion will lead to serious underregularization, particularly in regions where the structural contrasts are large.

Using wavenumber spectra of the measured signal, we can predict the nonlinearity noise variance. Tests demonstrate that reasonable regularization of the inverse problem results when this additional data error is taken into account.

For long profiles the algorithm presented speeds up the 2-D inversion by a factor of 100 000 relative to a single conventional linearized iterative step. Moreover, because the degree of added nonlinearity regularization adapts to local signal power, the output is an automated and effective resistivity estimate under the intrinsic limitations in a one-pass linear inversion of a nonlinear problem.

### FORMULATION OF THE MULTICHANNEL DECONVOLUTION

#### Theory

Geoelectric 2-D profile data, expressed as apparent resistivities  $\rho_a$ , are nonlinear functions of electrical resistivities  $\rho$ :

$$\rho_a(x, s) = g[\rho(x', z'), s] \quad s = s_1, s_2, \dots, s_S, \quad (1)$$

where  $g$  describes the earth response for this resistivity distribution to one out of  $S$  possible electrode configurations. The  $x$ -axis is assumed to be perpendicular to the strike direction, and the  $z$ -axis points downward.

Equation (1) can be expanded into a Taylor series with respect to a reference medium,  $\rho_{\text{ref}}$ :

$$\rho_a(x, s) = g[\rho_{\text{ref}}(x', z'), s] + \int_0^\infty dz' \int_{-\infty}^\infty \Phi(x', z', x, s) \times [\rho(x', z') - \rho_{\text{ref}}(x', z')] dx' + R, \quad (2)$$

where  $\Phi$  is the 2-D form of the Fréchet derivative evaluated for the reference medium and  $R$  is the second-order remainder.

The parameters are transformed logarithmically so that the parameter perturbation is

$$\delta m(x, z) = \log \rho(x, z) - \log \rho_{\text{ref}}(x, z). \quad (3)$$

Likewise, the data perturbation is

$$\delta d(x, s) = \log \rho_a(x, s) - \log g[\rho_{\text{ref}}(x', z'), s]. \quad (4)$$

The logarithmic transformation prevents nonphysical negative resistivities and makes the problem more linear because it equalizes large and small resistivity levels. The parameter perturbation [equation (3)] and the data perturbation [equation (4)] are inserted in equation (2). The Fréchet derivative for logarithmic data with respect to logarithmic parameters is given by

$$\frac{\partial \log \rho_a}{\partial \log \rho} = \frac{\rho}{\rho_a} \frac{\partial \rho_a}{\partial \rho}. \quad (5)$$

Note that for a homogeneous reference medium,  $\rho_a = \rho$ .

Ignoring the remainder term,  $R$ , in equation (2), the Born approximation is obtained (Boerner and West, 1989). When using a stratified reference medium, we obtain

$$\delta d(x, s) \simeq \int_0^\infty dz' \int_{-\infty}^\infty \Phi(0, z', x - x', s) \delta m(x', z') dx', \quad (6)$$

where the inner integral is a convolution between  $\Phi(0, z', \cdot, s)$  and  $\delta m(\cdot, z')$ . The value  $\Phi$  inherits the translational invariance of the reference medium—in this paper a homogeneous half-space. Expressions for the 2-D form of the Fréchet derivative appear in the following section.

Model parameterization,  $\delta m(x, z)$ , is discretized in terms of  $M$  layers; thereby the resistivities  $\rho(x, z)$  are approximated with functions  $\rho(x, l)$ , which describe the lateral variation in one layer. Under this discretization, equation (6) yields

$$\delta d(x, s) \simeq \sum_{l=1}^M \int_{-\infty}^\infty \tilde{\Phi}(x - x', l, s) \delta m(x', l) dx', \quad (7)$$

where

$$\tilde{\Phi}(x, l, s) = \int_{z_{l-1}}^{z_l} \Phi(0, z', x - x', s) dz'. \quad (8)$$

Expression (7) is a multichannel convolution when the lateral discretization and data in all electrode configurations are represented regularly along the profile.

Fourier transformation of expression (7) leads to a sum of products:

$$\tilde{\delta d}(k, s) \simeq \sum_{l=1}^M \tilde{\tilde{\Phi}}(k, l, s) \tilde{\delta m}(k, l), \quad (9)$$

where the wavenumber  $k = 1/\lambda$  is reciprocal wavelength and the tilde denotes Fourier domain variables.

For each wavenumber, equation (9) forms a linear system of equations:

$$\tilde{\delta \mathbf{d}}_k \simeq \tilde{\mathbf{G}}_k \tilde{\delta \mathbf{m}}_k + \tilde{\mathbf{e}}_k, \quad (10)$$

where  $\tilde{\delta \mathbf{d}}_k = [\tilde{\delta d}(k, 1), \dots, \tilde{\delta d}(k, s), \dots, \tilde{\delta d}(k, S)]^T$ ,  $\tilde{\delta \mathbf{m}}_k = [\tilde{\delta m}(k, 1), \dots, \tilde{\delta m}(k, l), \dots, \tilde{\delta m}(k, M)]^T$ , an entry in  $\tilde{\mathbf{G}}_k$  is  $\tilde{\tilde{\Phi}}_{kl} = \tilde{\tilde{\Phi}}(k, l, s)$ , and  $\tilde{\mathbf{e}}_k$  contains the Fourier transforms of the data errors. The linear system of equations in equation (10) can be regarded as a  $k$ -slice in a 3-D matrix as illustrated in Figure 1.

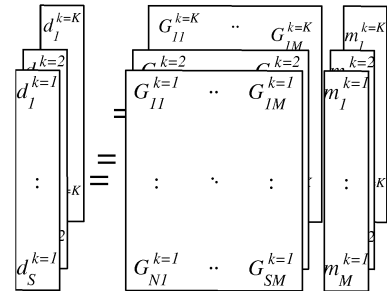


FIG. 1. Sketch of vectors and matrices forming the many small linear systems of equations [equation (10)] in the wavenumber domain.

Adopting the stochastic viewpoint (e.g., Jackson, 1979; Tarantola and Valette, 1982a), a solution to equation (10) becomes

$$\widetilde{\mathbf{m}}_k = (\widetilde{\mathbf{G}}_k^H \widetilde{\mathbf{C}}_{d_k}^{-1} \widetilde{\mathbf{G}}_k + \widetilde{\mathbf{C}}_{m_k}^{-1})^{-1} \widetilde{\mathbf{G}}_k^H \widetilde{\mathbf{C}}_{d_k}^{-1} \widetilde{\mathbf{d}}_k \quad (11)$$

where  $\widetilde{\mathbf{G}}_k^H$  is the hermitian form of  $\widetilde{\mathbf{G}}_k$ ,  $\widetilde{\mathbf{C}}_{d_k}$  is the data error covariance matrix describing the statistical variability of the data errors at this wavenumber  $k$ , and  $\widetilde{\mathbf{C}}_{m_k}$  is the model covariance matrix describing the statistical variability of the model perturbation,  $\widetilde{\mathbf{d}}_k$ .

The resulting resistivity estimate at a given depth  $z$  is

$$\rho(x, z) = \rho_{\text{ref}} \exp\{\mathcal{F}^{-1}[\widetilde{\mathbf{d}}m(k, z)]\}, \quad (12)$$

where  $\mathcal{F}^{-1}$  denotes inverse Fourier transformation in the horizontal direction.

### Fréchet derivative for 2-D resistivity data

The Fréchet derivative for the homogeneous half-space for the electrical potential  $V_{pp}$ , at  $P = (a, 0, 0)$  from a current injection at  $C = (0, 0, 0)$  is (see Boerner and West, 1989; Park and Van, 1991)

$$\begin{aligned} & \frac{\partial \Delta V_{pp}(0, a)}{\partial \rho(x', y', z')} \\ &= \frac{I}{4\pi^2} \frac{x'(x' - a) + y'^2 + z'^2}{(x'^2 + y'^2 + z'^2)^{3/2} [(x' - a)^2 + y'^2 + z'^2]^{3/2}}. \end{aligned} \quad (13)$$

Analytical integration of equation (13) in the  $y$ -direction, i.e., along strike, yields the 2-D form of the Fréchet derivative. We obtain for  $x' < a/2$

$$\begin{aligned} \frac{\partial \Delta V_{pp}(0, a)}{\partial \rho(x', z')} &= \frac{I}{2\pi^2 \beta} \left\{ \frac{\mathbf{K}(q_1) - \mathbf{E}(q_1)}{\beta^2 - \alpha^2} \right. \\ & \quad \left. - \frac{\alpha x' [(\beta^2 + \alpha^2)\mathbf{E}(q_1) - 2\alpha^2 \mathbf{K}(q_1)]}{\alpha^2(\beta^2 - \alpha^2)^2} \right\}; \end{aligned} \quad (14a)$$

for  $x' = a/2$ ,

$$\frac{\partial \Delta V_{pp}(0, a)}{\partial \rho(x', z')} = \frac{I}{8\pi} \left[ \frac{1}{(x'^2 + z'^2)^{3/2}} - \frac{3x'^2}{2(x'^2 + z'^2)^{5/2}} \right]; \quad (14b)$$

and for  $x' > a/2$ ,

$$\begin{aligned} \frac{\partial \Delta V_{pp}(0, a)}{\partial \rho(x', z')} &= \frac{I}{2\pi^2 \alpha \beta^2} \left\{ \frac{\alpha^2 \mathbf{E}(q_2) - \beta^2 \mathbf{K}(q_2)}{\alpha^2 - \beta^2} \right. \\ & \quad \left. - \frac{\alpha x' [(\alpha^2 + \beta^2)\mathbf{E}(q_2) - 2\beta^2 \mathbf{K}(q_2)]}{(\alpha^2 - \beta^2)^2} \right\}, \end{aligned} \quad (14c)$$

where  $\alpha^2 = x'^2 + z'^2$ ,  $\beta^2 = (x' - a)^2 + z'^2$ ,  $q_1 = \sqrt{(\beta^2 - \alpha^2)/\beta^2}$ ,  $q_2 = \sqrt{(\alpha^2 - \beta^2)/\alpha^2}$ , and  $\mathbf{K}$  and  $\mathbf{E}$  are the complete elliptical integrals of the first and second kind. Loke and Barker (1995)

reach similar expressions to equations (14a–c), except for misprints in the arguments of the elliptical integrals.

The potential for a four-electrode configuration is a sum of four pole–pole potentials so that the total 2-D Fréchet derivative is

$$\begin{aligned} \frac{\partial \Delta V_{4p}(x, s)}{\partial \rho(x', z')} &= \frac{\partial \Delta V_{pp}(0, x_M - x_A)}{\partial \rho(x' - x_A, z')} - \frac{\partial \Delta V_{pp}(0, x_N - x_A)}{\partial \rho(x' - x_A, z')} \\ & \quad - \frac{\partial \Delta V_{pp}(0, x_M - x_B)}{\partial \rho(x' - x_B, z')} + \frac{\partial \Delta V_{pp}(0, x_N - x_B)}{\partial \rho(x' - x_B, z')}, \end{aligned} \quad (15)$$

where  $x_A$  and  $x_B$  are current electrodes,  $x_M$  and  $x_N$  are potential electrodes,  $s$  is the index of the associated electrode configuration, and  $x$  is the reference position of the electrode configuration. Because apparent resistivity is expressed as

$$\rho_a = \frac{K}{I} \Delta V, \quad (16)$$

where

$$K = \frac{2\pi}{\frac{1}{|x_A - x_M|} - \frac{1}{|x_A - x_N|} - \frac{1}{|x_B - x_M|} + \frac{1}{|x_B - x_N|}},$$

the 2-D form of the Fréchet derivative for  $\rho_a(x, s)$  with respect to  $\rho(x', z')$  is

$$\Phi(x', z', x, s) = \frac{K}{I} \cdot \frac{\partial \Delta V_{4p}(x, s)}{\partial \rho(x', z')}, \quad (17)$$

which is the expression used in the multichannel deconvolution.

Figure 2 displays the 2-D form of the Fréchet derivative for the apparent resistivity for a pole–pole-like electrode array (configuration s6 in Figure 4), with the current electrodes placed at  $x = -15$  and  $15$  m and the potential electrodes placed at  $x = -25$  and  $45$  m.

### Fractal covariance model for subsurface resistivity

As already implicitly assumed in equation (11), we describe the spatial variation character of  $\log \rho(x, z)$  in the framework of stationary stochastic processes (e.g., Pilkington and Todoeschuck, 1990).

The degree of spatial correlation is parameterized in terms of fractal dimension  $D$  of a self-affine process, which is

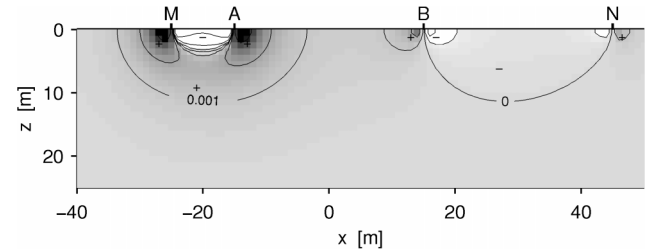


FIG. 2. 2-D form of the Fréchet derivative for an electrode configuration with current and potential electrodes placed at  $x = -15$  m (A),  $x = 15$  m (B),  $x = -25$  m (M), and  $x = 45$  m (N) (configuration s6 in Figure 4). Light gray indicates negative values; dark gray, positive values. Contour intervals are  $-0.010$ ,  $-0.003$ ,  $-0.001$ ,  $0$ ,  $0.001$ ,  $0.003$ ,  $0.010$ .

characterized by the von Kármán covariance functions

$$C(x, z, A, \nu) = A^2 C_0 \left(\frac{r}{L}\right)^\nu K_\nu(r/L), \quad (18)$$

where  $A$  is the amplitude,  $C_0$  is a constant,  $r = \sqrt{x^2 + z^2}$  is spatial distance,  $L$  is the correlation length, and  $K_\nu$  is the modified Bessel function of second kind and order  $\nu$ . The value  $C_0$  is selected so that  $A$  is the rms amplitude in the band  $4 \text{ m} \leq \lambda \leq 64 \text{ m}$ . We refer to  $A$  as the logarithmic amplitude of the resistivity and  $\nu$  as the shape parameter, which is related to the fractal dimension  $D$  as  $\nu = 3 - D$  (e.g., Maurer et al., 1998).

Prior knowledge on the presence of horizontal layering may be included by assuming a correlation length that is greater laterally than vertically. This will increase lateral coherence in the inversion result but will also reduce lateral resolution. Although layers are to be expected in sedimentary areas, this study uses an isotropic model covariance function so that a possible lateral coherence is purely data driven.

The 1-D auto and cross-spectra, which are analytically given cosine transforms of equation (18) and are required for equation (11), are [Erdélyi (1954), eqs. 1.13(45) and 1.12(41)]

$$\begin{aligned} \tilde{C}(k, z, A, \nu) &= \frac{A^2 C_0 \sqrt{\pi} |z|^{\nu+1/2}}{\sqrt{2} L^{2\nu} [1/L^2 + (2\pi k)^2]^{\nu/2+1/4}} \\ &\times K_{-\nu-1/2}[|z|\sqrt{1/L^2 + (2\pi k)^2}] \quad z \neq 0, \end{aligned} \quad (19)$$

$$\tilde{C}(k, 0, A, \nu) = \frac{A^2 C_0 \sqrt{\pi} 2^\nu \Gamma(\nu + 1/2)}{2L^{2\nu} [1/L^2 + (2\pi k)^2]^{\nu+1/2}} \quad \nu > -1/2. \quad (20)$$

Entry  $(i, j)$  in the model covariance matrix for the wavenumber  $k$  is given as  $\tilde{\mathbf{C}}_{m_k}(i, j) = \tilde{C}(k, z_i - z_j, A, \nu)$ . In this paper we use model covariance matrices with correlation length somewhat longer than the profile length ( $L = 1000 \text{ m}$ ) and varied  $\nu$  and  $A$ .

### Resolution test

Figure 3a displays a test model with resistivities that vary by a factor of 1.5 from the background value. Synthetic data for this low-contrast model were calculated using a finite-difference code (McGillivray, 1992). The same dense finite-difference mesh was used in all calculations, and testing for a homogeneous half-space model resulted in computation errors typically  $<0.5\%$  and globally  $<1.5\%$ . Data displayed in Figure 3b as an apparent resistivity pseudosection were calculated for eight Wenner configurations with electrode spacings between 2 and 32 m. The data pseudosection displays the characteristic pant legs anomaly pattern. This plotting artifact is also seen in the data pseudosection for pole-pole data with eight electrode spacings between 2 and 18 m (Figure 3c), but the pant legs are less recognizable in the data pseudosection for the Pulled Array Continuous Electrical Sounding (PACES) array in Figure 3d. The PACES array is built up around one set of current electrodes with 30-m spacing, using Wenner configurations and pole-pole-like configurations (Figure 4), so data collected

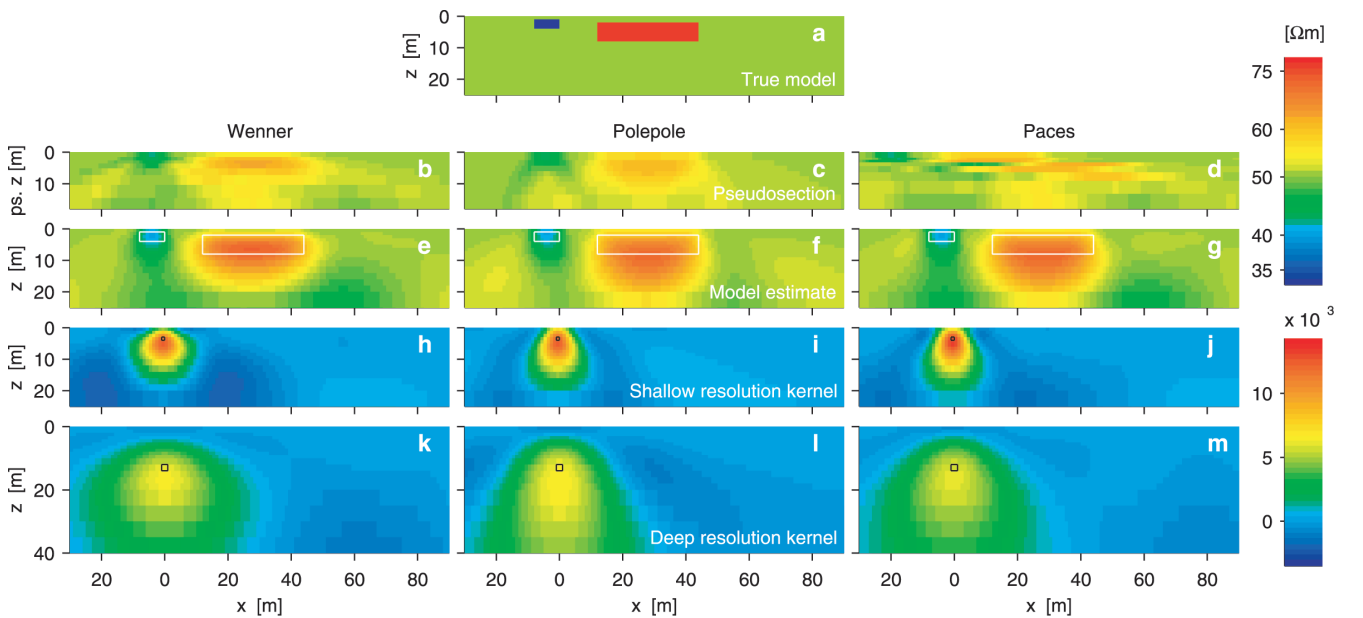


FIG. 3. Data pseudosections, model estimates, and model resolution kernels for data in Wenner, pole-pole, and PACES arrays. (a) True model with low-contrast anomalies; a small conductive block (33 ohm-m) and a larger resistive block (75 ohm-m) in a 50 ohm-m half-space. Apparent resistivity pseudosections for (b) Wenner configurations with electrode spacings 2, 4, 6, 8, 12, 16, 24, and 32 m; (c) pole-pole configurations with electrode spacings 2, 4, 6, 8, 10, 12, 14, and 18 m; and (d) PACES array (Figure 4). The depth conversion used in (b), (c), and (d) are equivalent to Edwards' (1977) median depth of investigations. Results of a multichannel deconvolution of the (e) Wenner, (f) pole-pole, and (g) PACES data, where the inverse operator uses  $\mathbf{C}_m$  described by an exponential correlation [ $\nu=0.5$  and  $A=0.05$  in equation (18)] and  $\mathbf{C}_d$  described by uncorrelated errors with  $\sigma=0.03$ . Corresponding model resolution kernels to the model estimates in (e), (f), and (g) for an element between 3 and 4 m [(h), (i), and (j)] and between 12 and 14 m [(k), (l), and (m)]. The upper colorbar maps colors for (a)-(g); the lower colorbar maps for (h)-(m).

simultaneously in all electrode configurations have different lateral focus. The data pseudosections are converted into approximate depth following Edwards' (1977) median depth of investigation defined as the depth, where the cumulative normalized 1-D form of the Fréchet derivative (Oldenburg, 1978) is 0.5.

Figures 3e–g show results of a multichannel deconvolution of the data displayed in Figures 3b–d, respectively. In all three cases, data are sampled every meter, meaning that the model partition consists of regular cells 1 m wide. The model is divided into 21 layers with layer thicknesses of 1 m for 0 to 10 m depth, 2 m for between 10 and 20 m depth, and 5 m down to 45 m depth. Beneath 45 m lies a basal half-space. The model estimates are achieved by assuming a model covariance matrix  $\mathbf{C}_m$ , describing an exponential correlation [ $\nu = 0.5$  and  $A = 0.05$  in equation (18)]. The data error covariance matrix,  $\mathbf{C}_d$ , describes uncorrelated errors with a standard deviation of 0.03, although for clarity the multichannel deconvolution is carried out on noise-free data in all three cases.

The model estimates in Figures 3e–g are more representative of the true model than are the pseudosections. The pole–pole case shows the best lateral resolution, and the Wenner case has better vertical resolution. The PACES case is intermediate.

These observations are confirmed by the model resolution kernels for a shallow and a deep cell in Figures 3h–m. In general, resolution diameter is proportional to focal depth, although the pole–pole kernel is slightly narrower and deeper than is the Wenner kernel. Again, the PACES case is intermediate.

### Nonlinearity error

Figure 5a shows the low-contrast model from Figure 3a together with a high-contrast model in which block resistivities differ by a factor of 10 from the reference half-space. Model responses are calculated for the PACES array. The thin curves in Figure 5b and c are the model responses of electrode configuration s6 with current and potential electrodes located at  $x = -15, 15, -25,$  and  $45$  m, respectively. The positive resistive anomaly seen in the data of electrode configuration s6 is shifted about 20 m to the right of the center of the causative body, representing the lateral focus of the configuration, which

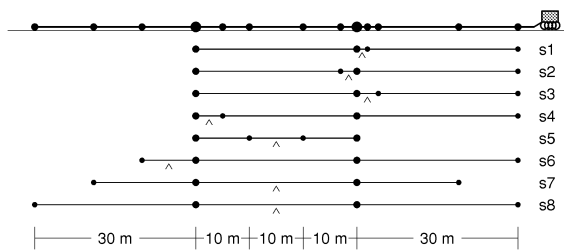


FIG. 4. PACES array. Sliding electrodes are mounted on a cable and towed by a small vehicle. The array has one set of current electrodes (larger  $\bullet$ ) separated by 30 m. Lines s1, s2, s3, s4, and s6 are pole–pole-like electrode configurations with pole–pole separations of 2, 3, 4, 5, and 10 m. Lines s5 and s8 are Wenner configurations with 10- and 30-m electrode spacings. Line s7 is a symmetric configuration with 19 m between current and potential electrodes. The  $\wedge$  marks the lateral focus of each electrode configuration. The Fréchet derivative of configuration s6 is shown in Figure 2.

is the area of the 2-D Fréchet derivative with most sensitivity (Figure 2).

The linear Born approximation response [equation (7)] for the low-contrast case (heavy curve in Figure 5b) agrees, within a fraction of 1%, with the full nonlinear response (thin curve). Thus, the Born approximation is valid for this low-contrast model.

In the high-contrast case, the differences between the linear Born approximation response (heavy curve in Figure 5c) and the nonlinear response (thin curve in Figure 5c) indicate a nonlinearity error well over 10%. As we invert nonlinear data with a linear inversion procedure, we regard the nonlinearity error as noise. Thus, in the high-contrast case the measurement noise is dominated by the nonlinearity noise, and we therefore suggest the nonlinearity error be taken into account as a part of the data errors (Tarantola and Valette, 1982b).

### Quantification of nonlinearity error variances

To develop regularization for nonlinearity error, a quantitative stochastic study of the nonlinearity error is required. Realizations of the resistivity distribution using the von Kármán family of covariance functions [equation (18)] are computed for three values of  $\nu$  (0, 0.25, and 0.5) and four values of  $A$  (0.1, 0.2, 0.5, and 1). Ten realizations of every parameter combination ( $\nu, A$ ) are computed using the same ten seeds in the random number generator. Nonlinear model responses of these 120 realizations are calculated for the PACES array shown in Figure 4, using the finite-difference code of McGillivray (1992). The nonlinearity error is defined as

$$e_{\text{non}} = \log(\rho_a^{\text{non}}) - \log(\rho_a^{\text{lin}}), \quad (21)$$

where  $\rho_a^{\text{non}}$  is the nonlinear response and  $\rho_a^{\text{lin}}$  is the approximate linear response given by the Born approximation. The

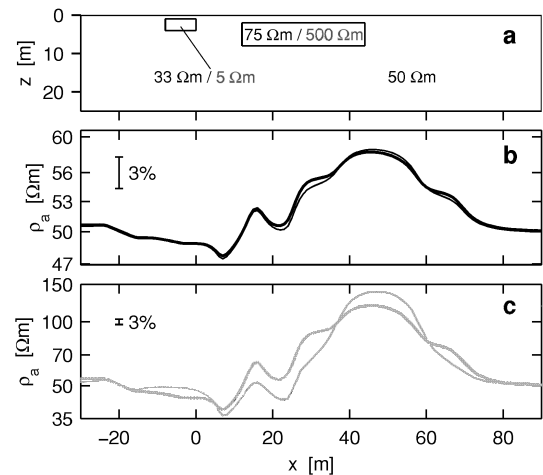


FIG. 5. PACES data in low- and high-contrast environments. True models with (a) low-contrast (as Figure 3a) and high-contrast anomalies with a small conductive block (5 ohm-m) and a larger resistive block (500 ohm-m) in a 50 ohm-m half-space. Model responses (b) and (c) are of PACES configuration s6 of the low-contrast model and the high-contrast model, respectively. The thin and heavy curves are nonlinear and linear model responses of the true models in (a), respectively.

stacked and smoothed autopower spectra of the nonlinearity error reveal power law decay above a corner wavenumber corresponding to a wavelength  $\lambda_{\text{corner}} \simeq 4z_f$  where  $z_f$  is the vertical focus depth [defined as Edwards' (1977) median depth of investigations] for the electrode configuration used. The nonlinearity error decay is almost parallel to the decay of the signal spectrum; for typical contrast levels the nonlinearity noise is unfortunately comparable in amplitude to the signal spectrum. Below the corner wavenumber the signal spectrum continues to rise toward smaller wavenumbers, whereas the nonlinearity noise tapers off into an almost constant level. These constant levels are well approximated by the expression

$$P_{\text{non}}(\nu, A, z_f) = cA^4 z_f^{(4\nu+2)}, \quad (22)$$

where  $c$  is a constant scale factor. The factor  $A^4$  is to be expected in the power spectrum because the remainder term in the Born approximation is second order. The dependence on focus depth,  $z_f$ , is perhaps less easy to predict. The nonlinearity error autopower enters into the total error covariance matrix as

$$\tilde{\mathbf{C}}_{d_k} = \tilde{\mathbf{C}}_{d_k}^{\text{meas}} + \tilde{\mathbf{C}}_{d_k}^{\text{non}}. \quad (23)$$

This formulation would allow a detailed specification of both autopower and cross-power spectra of both the measurement noise and the nonlinearity noise.

Examples presented in this paper approximate  $\tilde{\mathbf{C}}_{d_k}^{\text{non}}$  as a diagonal matrix with diagonal elements independent of  $k$  but varying as  $P_{\text{non}}(\nu, A, z_f)$  in equation (22). Because the nonlinearity error decreased above the corner wavenumber, our approximation is conservative. Note that the nonlinearity error expressions share the amplitude  $A$  and the shape parameter  $\nu$  with the model covariance expressions. For consistency, the same  $A$  and  $\nu$  control both  $\mathbf{C}_m$  and  $\mathbf{C}_d^{\text{non}}$  in the following.

Actual measurement noise, though small in general, may well increase with increasing electrode separation. For pulled arrays (see Figure 4) some crosscorrelation would be expected where different configurations share some of the moving electrodes. However, rarely are we able to quantify these noise characteristics. Therefore, in this study we assume the measurement error to be white and equal in all electrode configurations; hence,  $\tilde{\mathbf{C}}_{d_k}^{\text{meas}}$  is diagonal with constant elements  $\sigma(\tilde{\epsilon}_{\text{meas}})^2$ .

### Estimation of $(\nu, A)$

When electrical well logs are abundant, it is possible to estimate values for  $A$  and  $\nu$  by variogram fitting. In practice, electrical profiling is often meant to reduce the drilling costs, so independent estimates of  $A$  and  $\nu$  are difficult to obtain.

However, representative values for  $A$  and  $\nu$  may be estimated from the electrical profile directly. Since the overall signal amplitude is proportional to  $A$  and because the shape parameter  $\nu$  controls the amplitude ratio between long and short wavelengths, these two stochastic parameters may be derived from apparent resistivity variance estimates in two wavelength bands.

Based on synthetic tests on responses from resistivity realizations with known  $A$  and  $\nu$ , we found the following empirical equations for apparent  $\nu$ ,

$$\nu_{\text{app}} = 1 - 0.9 \frac{\text{rms}_{\text{short}}}{\text{rms}_{\text{long}}}, \quad (24)$$

and for apparent  $A$ ,

$$A_{\text{app}} = 14(\text{rms}_{\text{short}} + \text{rms}_{\text{long}}), \quad (25)$$

where  $\text{rms}_{\text{short}}$  and  $\text{rms}_{\text{long}}$  are root-mean-square amplitudes for signals in bands  $\lambda \in [4, 16]$  m and  $\lambda \in [16, 64]$  m stacked from four intermediate electrode configurations of the PACES array (s3, s4, s5, and s6 in Figure 4). For other choices of electrode arrays and wavelength bands, expressions for apparent  $A$  and  $\nu$  may require modification.

Figure 6 shows the running estimate of  $\nu_{\text{app}}$  and  $A_{\text{app}}$  for data which are responses of realizations of von Kármán covariance functions. The estimates seem unbiased and agree satisfactorily with the true values. The rms running averages were computed using a 100 m interval. Longer running average intervals would give more stable values of  $A_{\text{app}}$  and  $\nu_{\text{app}}$  but would also smear possible boundaries where the properties of the electrofacies change.

### SYNTHETIC EXAMPLE

In this example, the data error covariance matrix specified in the previous section is included in the inverse operator of the multichannel deconvolution [equation (11)]. The attributes  $\nu$  and  $A$  are estimated using the empirical equations (24) and (25).

Figure 7a displays part of a stochastic resistivity structure, which is a realization of the covariance function [equation (18)] with the parameters  $A = 0.5$  and  $\nu = 0.25$ . The corresponding model responses, computed for the PACES array, are displayed as an apparent resistivity pseudosection in Figure 7b. Model responses for the individual electrode configurations are plotted

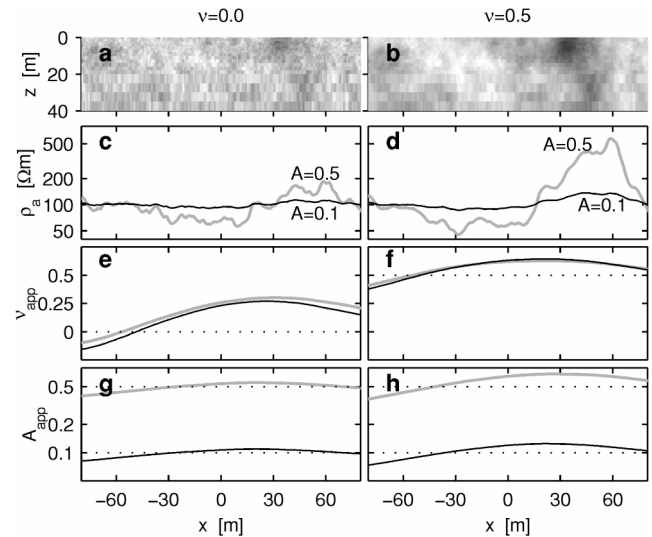


FIG. 6. Estimation of  $\nu_{\text{app}}$  and  $A_{\text{app}}$ . Realization of a stationary process with von Kármán covariance functions [equation (18)] with  $L = 1000$  m; (a)  $\nu = 0$  and (b)  $\nu = 0.5$ . Model responses for PACES configuration s6 of the von Karman realizations in (a) and (b) with  $A = 0.1$  (black curves) and  $A = 0.5$  (heavy gray curves) are shown for (c)  $\nu = 0$  and (d)  $\nu = 0.5$ . Apparent  $\nu$  estimated from the model responses in (c) and (d) is plotted in (e) and (f), respectively. Corresponding apparent  $A$  is plotted in (g) and (h).

at the lateral focus points (marked in Figure 4), defined as

$$x_f = \begin{cases} (x_c + x_p)/2 & \text{if pole-pole-like configuration} \\ (x_A + x_B)/2 & \text{if symmetric configuration} \end{cases}, \quad (26)$$

where  $x_c$  and  $x_p$  are the pole-pole-like electrodes to make the data pseudosection informative. Running estimates of apparent  $\nu$  and  $A$  (Figure 7d) for these data show a  $\nu_{app}$  undulating around 0.25 and an  $A_{app}$  around 0.5. A model estimate of data with 3% white noise is displayed in Figure 7e, which is a result of a multichannel deconvolution using an inverse operator with covariance matrices that are controlled by the true values of  $\nu$  (0.25) and  $A$  (0.5). The model estimate gives a blurred image, especially at depth, but many details are still recovered in the upper layers. The apparent resistivity response of the model estimate (Figure 7c) shows good agreement with the data (Figure 7b).

### FIELD EXAMPLES

Field data only approximately satisfy the requirements for the multichannel deconvolution. Spatial sampling is often irregular, and field data are not periodic. Regular sampling is achieved through interpolation. Periodicity is imposed through padding and periodic interpolation. To minimize end effects, the total padding length must be larger than the length of the largest electrode configuration.

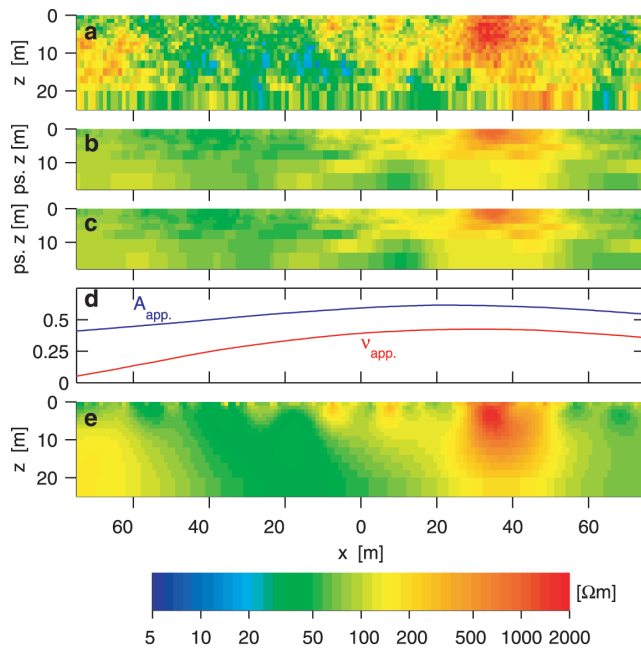


FIG. 7. A stochastic resistivity structure resulting from a realization of equation (18) for  $\nu = 0.25$  and  $A = 0.5$  is used as the true model (a). Model responses computed for the PACES array are displayed as an apparent resistivity pseudosection (b) shifted laterally according to equation (26) and converted into depth as in Figure 3. (c) The model response of the model estimate in (e). (d) The estimated apparent  $\nu$  and  $A$  for the data in (b). (e) The model estimate from data with 3% white noise obtained by an inverse operator controlled by  $\nu = 0.25$  and  $A = 0.5$ .

### PACES data from Ølst

With the PACES method (Sørensen, 1996; Møller et al., 1998), more than 30 profile kilometers of data covering about 12 km<sup>2</sup> were collected in an exploration for smectite-rich clay. Upper Paleocene clay from the Ølst Formation (Heilmann-Clausen et al., 1985) is exposed in hills formed by glaciotectionics at Ølst, Jutland, Denmark. The heavily disturbed clay deposits are surrounded by glaciofluvial sand and gravel deposits and are overlain by a thin, clayish till (Nielsen, 1973).

Multichannel deconvolution was applied to data profiles with typical lengths of 900 m. A 150-m interval is displayed in Figure 8a as a resistivity pseudosection shifted laterally according to equation (26) and converted into depth. From the estimated apparent  $\nu$  and  $A$  (Figure 8c), a  $\nu = 0.60$  and an  $A = 0.4$  are picked to control the inverse operator. Figure 8d displays part of the model estimate.

The response of the model estimate in Figure 8d (Figure 8b) generally agrees with the measured data (Figure 8a) but indicates that the transition between low and high resistivities between 440 and 460 m is even sharper than that obtained in the model estimate.

Resistivities above 100 ohm-m are interpreted to be dry glaciofluvial sand and gravel, resistivities below 5 ohm-m are interpreted to be Palaeocene clay, and the intermediate resistivities at about 30 ohm-m are interpreted to be a clayish till. The almost vertical contact between clay and sand can be followed in adjacent lines supporting the assumption of a 2-D structure with strike direction perpendicular to the profile.

### CVES data from Grundfør

Profiles of continuous vertical electrical sounding (CVES) data were collected at Grundfør, Jutland, Denmark, as part of a larger groundwater project under the Danish Environmental Research Programme. In these projects, the Quaternary aquifers that exist in buried valleys incised into Tertiary clay deposits were mapped and studied.

Using the ABEM Lund imaging system (Dahlin, 1996), data were collected in Wenner configurations with 10-electrode spacings between 5 and 120 m. Figure 9a displays data from the central profile. A model estimate is obtained using an inverse operator controlled by  $\nu = 0.65$  and  $A = 0.25$  (read from Figure 9c). The rectangles indicate four Ellog drillings, which were <10 m offline. The Ellog method is based on an electrical log and a gamma log measured continuously while drilling (Sørensen, 1989). The augering method uses no drilling mud and provides a relatively undisturbed estimate of the true formation resistivity. The measured resistivities are indicated as color in the rectangles in Figure 9d. Thin beds present in the logs are not resolvable with surface electrical methods. Therefore, we judge the correspondence between the Ellog resistivity and the resistivities obtained by the multichannel deconvolution to be satisfactory.

The profile displayed in Figure 9 maps a cross-section of the sediments that have filled and covered a buried valley, known to cut about 120 m into Tertiary clay. The valley is about 1 km wide, and its slopes are outside the profile. The low (about 25 ohm-m) and intermediate (about 40 ohm-m) resistivities in the lower part of the section are interpreted as clay and more

coarse-grained sediments deposited in a glaciolacustrine environment (Gravesen, 1997). The upper part of the section dominated by higher resistivities is interpreted as glaciofluvial sand and gravel deposited in front of the latest glacial advance, which

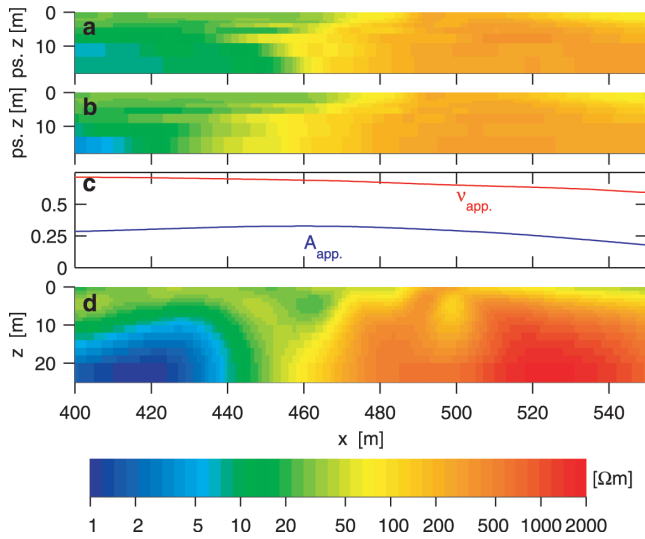


FIG. 8. Data collected using the PACES method at Ølst are displayed as an apparent resistivity pseudosection (a) shifted laterally according to equation (26) and converted into depth as in Figure 3. (b) The model response of the model estimate in (d). (c) The estimated apparent  $\nu$  and  $A$  from the data in (a). (d) The model estimate obtained by an inverse operator controlled by  $\nu = 0.60$  and  $A = 0.4$ .

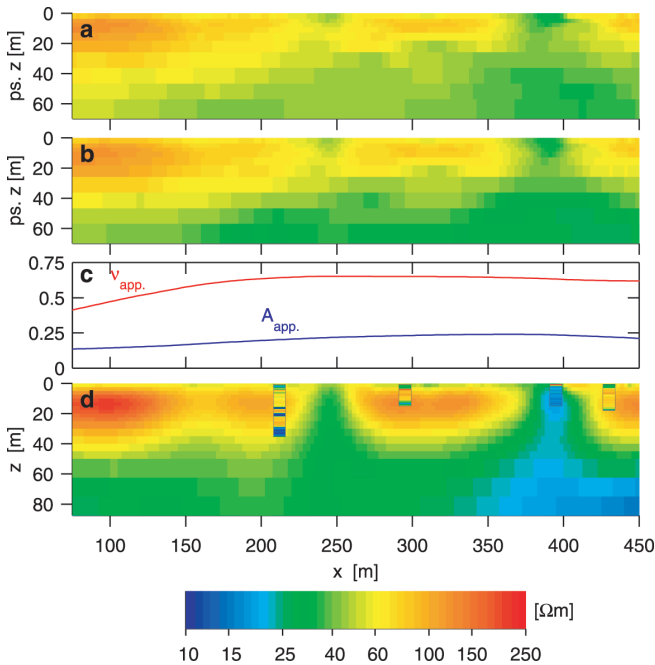


FIG. 9. Data collected at GrundfØr using Wenner configurations with electrode spacings between 5 and 120 m are displayed as an apparent resistivity pseudosection (a) converted into depth as in Figure 3. (b) The model response of the model estimate in (d). (c) The estimated apparent  $\nu$  and  $A$  from the data in (a). (d) The model estimate obtained by an inverse operator controlled by  $\nu = 0.65$  and  $A = 0.25$ . The small rectangles in (d) indicate the location of electrical resistivity logs, which are displayed as color in the rectangles.

deposited a thin, incoherent till (resistivities about 40 ohm-m) seen as the topmost deposit in the section.

## DISCUSSION

### Implementation aspects and performance

The 2-D Fréchet derivative, which is relatively expensive to compute, is calculated once and stored for each electrode array and profile sampling. The model covariance matrices are also calculated in advance for unit amplitude and a suite of different values of the shape parameter  $\nu$ . Various tests show that model estimates of the same data set obtained using slightly different  $\nu$  are almost the same, indicating the shape parameter can be sampled rather coarsely, e.g., in steps of 0.25. The nonlinearity error variance  $\mathbf{C}_d^{\text{non}}$  is rapid to compute and does not have to be stored in advance.

The algorithm is developed as a Matlab script, which leaves room for computational optimization. Still, estimation of 10 752 ( $512 \times 21$ ) model parameters through a multichannel deconvolution of 4096 ( $512 \times 8$ ) data values demands  $<2$  MB of memory and requires 0.2 s on a 400-MHz Pentium II computer. The solution of the same problem (10 752 model parameters and 4096 data values) set up as  $\mathbf{m}_{\text{est}} = \mathbf{C}_m \mathbf{G} (\mathbf{G} \mathbf{C}_m \mathbf{G} + \mathbf{C}_d)^{-1} \mathbf{d}_{\text{obs}}$  in the space domain and solved using a Cholesky factorization of  $\mathbf{G} \mathbf{C}_m \mathbf{G} + \mathbf{C}_d$  would demand 1.3 GB of memory and would take about 20 hours of computer time.

### Nonlinearity error regularization

A one-pass inversion with a data error covariance matrix accounting for, say, 1% measurement noise may lead to dramatically underregularized results. We suggest that the nonlinearity error be taken into account as an additional error covariance matrix, with diagonal elements given by equation (22). A coarser approximation would be to scale the constant diagonal measurement error covariance matrix. This would be the result in a Tichonov or Occam approach, where a free regularization parameter is adjusted until some criterion is fulfilled. For this choice of nonlinearity regularization, Møller (1999) found significantly poorer test results. The actual nonlinearity noise spectrum was found to decrease at higher wavenumbers. Møller (1999) did not find significant differences between estimates which took this decay into account and estimates based on the conservative constants in equation (22).

Multichannel deconvolution is most suitable for inversion of long profiles. Profile lengths shorter than three times the longest electrode separation give rise to model estimates needing extra stabilization in the lower part of the model.

### Should regularization be adaptive?

Elementary statistical theory states that the expected value and variance of a series of repeated measurements is computed from the average and the deviations from the average. Moreover, expressions for the confidence interval of the true expectation value may be based on these estimates of expectation value and variance. We view the empirical equations (24) and (25) for estimates of parameters  $A$  and  $\nu$  in the same spirit. When the subsurface resistivity distribution is a realization of a von Karman process [see equation (18)],  $A_{\text{app}}$  and  $\nu_{\text{app}}$  will only be approximate, as seen in Figure 6, and therefore the resulting regularization may be slightly suboptimal. The theoretical

argument for adaptive regularization is weaker when the actual resistivity distribution is likely not a von Karman realization. We were therefore surprised to see how well adaptive regularization worked even for highly nonstochastic and rather unrealistic synthetic models like Figure 3 (Møller, 1999) as well as for typical field cases.

This study considers electrode spacings with focus depths  $z_f$  between 1 and 16 m. Nonlinearity errors as well as apparent  $A$  and  $\nu$  are measured from data in the band  $4\text{ m} \leq \lambda \leq 64\text{ m}$ . When other electrode spacings with other focus depths are used, we suggest measuring apparent  $A$  and  $\nu$  in the band  $\bar{z}_f \leq \lambda \leq 16\bar{z}_f$ , where  $\bar{z}_f$  is the geometric mean of all focus depths.

### Practical combination of automated multichannel deconvolution and nonlinear inversion

Multichannel deconvolution gives a first-order interpretation of large sets of profile data. The empirical equations (24) and (25) for apparent  $A$  and  $\nu$  allow for automated multichannel deconvolution. Both synthetic and field examples have shown that the estimated apparent  $A$  and  $\nu$  lead to reasonable model estimates, and only rarely did changes from these values lead to significantly better or more reliable results.

From the initial deconvolution, sections with small apparent amplitude variations will be accepted as almost linear, while sections with larger apparent amplitude will be interpreted by means of an iterative inversion. Sections with only 1-D structures will be interpreted with 1-D inversion schemes.

### CONCLUSIONS

We have presented a one-pass 2-D inversion algorithm formulated as a multichannel deconvolution using the 2-D Fréchet derivative for the homogeneous half-space. Because the multichannel deconvolution is solved in the wavenumber domain, the algorithm is fast and memory efficient.

The inversion is regularized through covariance matrices reflecting the stochastic properties of the earth resistivity and data errors. A nonlinearity error covariance matrix is added to the conventional measurement error covariance matrix.

The stochastic properties of the nonlinearity error are derived from a nonlinear simulation experiment. An empirical expression is derived for predicting nonlinearity error variances for given resistivity amplitude and fractal dimension in a self-similar stochastic model for resistivity distribution. Moreover, expressions are derived for estimating apparent amplitude and fractal dimension of the logarithmic resistivity distribution directly from measured apparent resistivity data. The combination of these elements defines an inversion procedure where regularization of the nonlinearity error adapts to the general resistivity amplitude level.

Both synthetic tests with known resistivity structure and a field test with electrical well-log control support the conclusion: for long data profiles, this method produces excellent linearized resistivity estimates.

### ACKNOWLEDGMENTS

All forward modeling was done using a finite-difference code kindly made available to us by Doug Oldenburg, The University of British Columbia. We thank Kurt Sørensen and Esben Auken, University of Aarhus, for making the field data available. The data from Ølst were collected for Aarhus County.

Collection of CVES and Ellog data in Grundfjør were carried out under the Groundwater Group of The Danish Environmental Research Programme.

Moreover, we thank reviewers David Boerner, Yaoguo Li, and Mark Goldman for many important remarks which helped us improve clarity and focus of this paper.

### REFERENCES

- Boerner, D. E., and West, G. F., 1989, Fréchet derivatives and single scattering theory: *Geophys. J. Internat.*, **98**, 385–390.
- Christensen, N. B., and Sørensen, K. I., 1998, Surface and borehole electric and electromagnetic methods for hydrogeological investigations: *Eur. J. Environ. Eng. Geophys.*, **3**, 75–90.
- Dahlin, T., 1996, 2D resistivity surveying for environmental and engineering applications: *First Break*, **14**, 275–283.
- Edwards, L. S., 1977, A modified pseudosection for resistivity and IP: *Geophysics*, **42**, 1020–1036.
- Erdélyi, A., 1954, *Table of integral transforms*, vol. I: McGraw-Hill Book Company, Inc.
- Gravesen, P., 1997, Three-dimensional geological model of the complex aquifers in an incised Quaternary valley in Jutland, Denmark: 3rd Meeting, *Environ. Eng. Geophys. Soc.*, Proceedings, 229–232.
- Griffiths, D. H., and Turnbull, J., 1985, A multi-electrode array of resistivity surveying: *First Break*, **3**, 16–20.
- Heilmann-Clausen, C., Nielsen, O. B., and Gersner, F., 1985, Lithostratigraphy and depositional environments in the Upper Paleocene and Eocene of Denmark: *Bull. Geol. Soc. Denmark*, **33**, 287–323.
- Jackson, D. D., 1979, The use of a priori data to resolve nonuniqueness in linear inversion: *Geophys. J. Roy. Astr. Soc.*, **57**, 137–157.
- LaBrecque, D. J., Miletto, M., Daily W., Ramirez, A., and Owen, E., 1996, The effects of noise on Occam's inversion of resistivity tomography data: *Geophysics*, **61**, 538–548.
- Li, Y., and Oldenburg, D. W., 1992, Approximate inverse mapping in DC resistivity problems: *Geophys. J. Internat.*, **109**, 343–362.
- Loke, M. H., and Barker, R. D., 1995, Least-squares deconvolution of apparent resistivity pseudosection: *Geophysics*, **60**, 1682–1690.
- Maurer, H., Holliger, K., and Boerner, D. E., 1998, Stochastic regularization: Smoothness or similarity?: *Geophys. Res. Lett.*, **25**, 2889–2892.
- McGillivray, P. R., 1992, Forward modeling and inversion of DC resistivity and MMR data: Ph.D. thesis, Univ. of British Columbia.
- Møller, I., 1999, Fast 2D inversion of large geoelectrical data sets for near-surface resistivity mapping: Ph.D. thesis, University of Aarhus, Denmark.
- Møller, I., and Sørensen, K. I., 1998, A new approach for fast 2D geoelectrical mapping of near-surface structures: *Eur. J. Environ. Eng. Geophys.*, **2**, 247–261.
- Møller, I., Sørensen, K. I., and Christensen, N. B., 1998, DC-resistivity multi-electrode profiling in hydrogeological investigations: A comparative study of the pulled array continuous electrical sounding method and a multi-electrode method with fixed electrodes: SAGEEP 1998 Conference, *Environ. Eng. Geophys. Soc.*, Proceedings, 869–874.
- Nielsen, O. B., 1973, Eocæne aflejringer i Ølst-området og deres indpasning i områdets Kvartærgeologi (Eocene deposits in the Ølst area and their fit in the quaternary geology of the area): *Dansk Geologisk Forening, Årskrift for 1972*, 100–110.
- Oldenburg, D. W., 1978, The interpretation of direct current resistivity measurements, *Geophysics*, **43**, 610–625.
- Panissod, C., Dabas, M., Hesse, A., Jolivet, A., Tabbagh, J., and Tabbagh, A., 1998, Recent developments in shallow-depth electrical and electrostatic prospecting using mobile arrays: *Geophysics*, **63**, 1542–1550.
- Park, S. K., and Van, G. P., 1991, Inversion of pole-pole data for 3-D resistivity structure beneath arrays of electrodes: *Geophysics*, **56**, 951–960.
- Pilkington, M., and Todoeschuck, J. P., 1990, Stochastic inversion for scaling geology: *Geophys. J. Internat.*, **102**, 205–217.
- Sasaki, Y., 1989, Two-dimensional joint inversion of magnetotelluric and dipole-dipole resistivity data: *Geophysics*, **54**, 254–262.
- Sørensen, K. I., 1989, A method for measurement of the electrical formation resistivity while auger drilling: *First Break*, **7**, 403–407.
- , 1996, Pulled array continuous electrical profiling: *First Break*, **14**, 85–90.
- Tarantola, A., and Valette, B., 1982a, Generalized nonlinear inverse problems solved using the least squares criterion: *Rev. Geophys. and Space Physics*, **20**, 219–232.
- , 1982b, Inverse problems: Quest of information: *J. Geophys.*, **50**, 159–170.